GRADIENT-INDEX METAMATERIAL INFRARED DETECTOR FOR ENHANCED PHOTO-RESPONSE AND IMAGE QUALITY

Kelsa Derek Adams

Thesis Prepared for the Degree of

MASTER OF SCIENCE

UNIVERSITY OF NORTH TEXAS

May 2022

APPROVED:

Richard Zhang, Major Professor
Hamid Sadat, Committee Member
Hassan Qandil, Committee Member
Herman Shen, Chair of the Department of Mechanical Engineering
Hanchen Huang, Dean of the College of Engineering
Victor Prybutok, Dean of the Toulouse Graduate School

Adams, Kelsa Derek. *Gradient-Index Metamaterial Infrared Detector for Enhanced Photo-Response and Image Quality*. Master of Science (Mechanical and Energy Engineering), May 2022, 36 pp., 2 tables, 12 figures, 59 numbered references.

An enhanced thermal imaging concept made possible through the development of a gradient-indexed metamaterial infrared detector that offers broadband transmission and reflection in THz waves. This thesis proposes a proof of feasibility for a metamaterial infrared detector containing an anti-reflective coating with various geometrically varying periodic metasurfaces, a gradient-indexed dielectric multilayer for near-perfect longpass filtering, and a gradient index of refraction (GRIN) metalens for enhanced focal plane thermal imaging. 2D Rigorous Coupled-Wave Analysis (RCWA) is used for understanding the photonic gratings performance based on material selection and varying geometric structure. Finite Difference Time Domain (FDTD) is used to characterize performance for a diffractive metalens by optimizing the radius and arrangement of cylindrical nanorods to create a desired phase profile that can achieve a desired focal distance for projections on a detector for near- to far-infrared thermal imaging. Through combining a micromachined anti-reflective coating, a near-perfect longpass filter, and metamaterial GRIN metalens, infrared/THz focal plane thermal imaging can obtain faster photo-response and image quality at targeted wavelengths, which allows for scientific advancements in electro-optical devices for the Department of Defense, aerospace, and biochemical detection applications.

TABLE OF CONTENTS

Page

LIST OF TABLES AND FIGURES

Page

Tables

Figures

CHAPTER 1

INTRODUCTION

1.1 Topic Overview

Infrared (IR)/terahertz thermal imaging capabilities are critical for scientific and engineering advancement as they can provide understanding about the Earth's surface and atmosphere, improve strategies for space exploration, and enhance our nation's defense. Optical remote-sensing technologies are in a great need for electro-optical devices to become smaller, less complex, and cheaper to manufacture. When optical devices meet these three characteristics, they lean towards becoming commercial off-the-shelf components, which help pave the way for new research studies constricted by budget, space, and availability. However, it is important when trying to overcome the size, weight, complexity, and price-point issues that the infrared imaging performance isn't compromised [1].

The evolution of infrared imaging systems is largely due to the advancements in new metamaterial compositions and nano/micromaterial fabrication techniques. Unique metamaterial compositions, such as potassium bromide (KBr) and polyvinyl chloride (PVC), allow for advanced performance in various applications due to their optical properties. Some material compositions like PVC offer unique fabrication opportunities due to their malleability, which can allow for easier production at a larger scale. As new metamaterial compositions become available, high-precision fabrication techniques will be needed to create complex geometries at various thicknesses. While the application for each device may be different, the end goal of designing a compact, lightweight, power conscious, and cost-effective mechanism remains the same.

Over the years, many scientific researchers have been consistently working to meet

challenges that IR systems still encounter today. For example, many infrared detectors require some sort of cooling to reduce thermal noise. While there are commercialized technologies that are uncooled, work at room temperature, and are low cost, the most prominent uncooled FPA is bolometer based [2-5]. However, it still suffers from fabrication challenges, slow response, and is susceptible to temperature variations [6]. Fabrication challenges can drive up manufacturing costs, which can limit the number of customers that are able to afford it. Slow response times will limit where the IR system can be utilized. For example, the Department of Defense will most likely not consider an IR system with a slow response time for aerospace applications due to safety concerns for their pilots in mission critical environments. IR systems that are susceptible to temperature variations without cooling are not practical for many applications because of their unfavorable image resolution and slow response time.

The Origins Space Telescope (Origins) is a mid-infrared detector that uses a spectrometer instrument designed to detect and measure the spectral signatures of gases of biogenic origins in the atmosphere, and studies the existence of known and unknown exoplanets [7]. One of the critical requirements for the Origins telescope is that it must remain stable due to the sensitivity requirements. High-stability detection must meet specific requirements, which include decreasing the noise, reducing stray capacitances, shorts, or crosstalk between circuits, improving pixel-to pixel uniformity, and optimizing the pixel pitch based on the final design [7]. Detector sensitivity is important to knowing and understanding what is going on around us, and it is only made possible through having a high-stability detector that is optimized based the previous requirements. Future research may find alternate ways of optimizing IR detectors to become highly stable by discovering new metamaterials, alternate designs, or from newfound cooling methods.

Depending on the application of the IR system, design tradeoffs must be carefully analyzed to determine the best way to optimize the design for its function. In most cases, IR system requirements are not as important to those with a different application. For example, photon detectors work through photon absorption of semiconductors, while thermal detectors absorb incident radiation that increase the temperature of the device [8]. Thermal detectors work at room temperature but may require bolometers to increase responsivity. In addition, antennas can be utilized to further enhance imaging performance in highly degraded environments by taking advantage of electromagnetic (EM) waves [8].

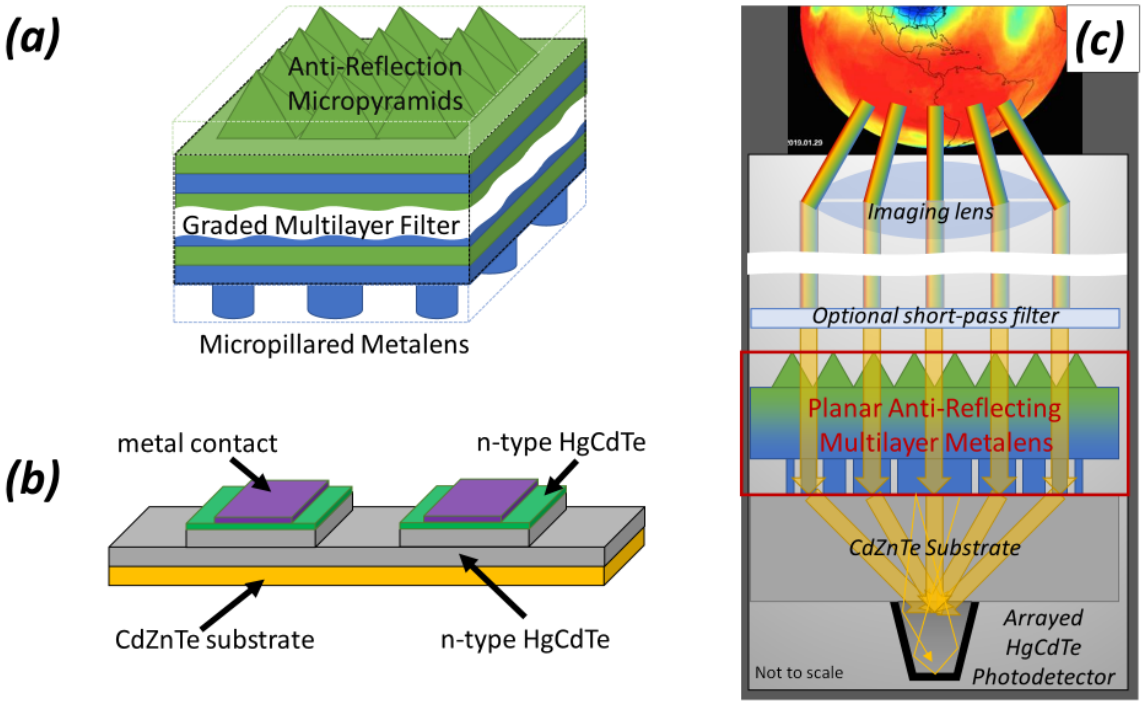

Figure 1: **Graphical representation of (a) planar anti-reflecting multilayer metalens integrated into an infrared device, (b) HgCdTe p-on-n photodiode photodetector, and (c) overall integrated design concept.**

Figure 1 shows how the proposed gradient-index multilayer metalens would integrate into the overall infrared detecting device. Due to the overall size of this infrared detector, the need for a thermal control component is not needed.

1.2 State of the Art Review

Modern electro-optical systems have a need for highly transparent, compact, and affordable anti-reflection coatings (ARC) in the near- to far-infrared wavelengths. The use of electro-optical ARC technology is seen in both commercial and defense industries. Some of the different applications are used to enhance imaging and remote sensing applications. For example, smart windows were developed to increase building performance by applying a thermochromic glazing, which regulates solar irradiation indoor protection. However, there is a trade-off between balancing luminous transmittance and solar modulating capabilities [9-11]. Biochemical detection has become increasingly important in remotely monitoring oil and gas facilities for leaks, non-invasive disease diagnosis, and environmental monitoring [12, 13]. Satellite-based detection has provided a cost effective and more frequent method of determining the state of each oil and gas facility. The performance of these satellite-based detectors has increased through the use of ARC's that help mitigate stray light, ghosting, radiation, and spectral bandpass inefficiencies [12]. Astrophotonic object detection seeks to discover and understand the atmospheres of rocky exoplanets and potential habitability by using space-based nulling interferometry [14, 15]. Space-based nulling interferometry could be utilized on CubeSats as well as larger vessels depending the on the mission. Light detection and ranging (LiDAR) utilizes attenuation and time-of-flight measurements of light pulses through the atmosphere to determine standoff detection for chemical species at a gaseous phase, and it can also be used for mobile robots that rely on depth completion tasks to better understand their surroundings [16, 17]. Furthermore, satellite-based infrared imaging systems, such as the US early warning satellite, monitors and detects enemy missiles and will issue incoming warnings, and can cover many different working bands [18]. Depending on the working band, these light detectors can

identify missile bases and types, launch reconnaissance, tracking, and can even enable visible light detectors to detect through clouds with the use of an atomic resonance filter [18]. There are abundant other possibilities that come from exploring new micro-manufacturing processes and optical material compositions for IR systems. By improving these applications, new configurations and designs can produce near-perfect quasioptical EM wave coupling with minimal absorption in the THz waves/infrared wavelengths. These new developments will pave the way and accelerate research in the future.

In previous works, different material compositions have been analyzed for the various applications listed above, but they are often limited in their transmissive capabilities, size requirements, and their simultaneously complex material mixtures, fabrication techniques, and thermal regulation properties [9, 19-25]. Highly transmissive and low absorption quasioptical ARC in the broad infrared spectrum is constrained by material selection and surface microstructure profile, which is largely due to the refractive index of the material. Various approaches have been made toward ARC applications, which include nature inspired microstructures. Moth-eye inspired nanopillar-type structure has influenced many researchers in developing anti-reflective surfaces for IR optical system enhancements [19, 20, 26, 27]. A telescope observatory developed an array of pyramidal structures made of microwave-transparent metamaterial layers constructed of carbon-loaded polyurethane on a tilted surface [24]. In addition, these pyramidal structures were made through injection molding, which enables mass production and lowers overall cost. Furthermore, these pyramidal array ARC concepts were aimed at suppressing stray light by minimizing reflection and scattering, which proved to have a reflectance of less than 1% up to a 65° angle of incidence [24, 26]. ARC concepts have also been applied to the area of smart windows, where there is a need for boosting

luminous transmittance while blocking stray thermal leakage [9]. Chip-scale perfectly transmitting high contrast gratings harnessed the concept of phase-matched waves, which have been used in vertical cavity surface emitting lasers [28]. Through careful periodic surface structure nano- to micro-patterning, various mechanisms can induce perfect transmission with select materials, which can be seen in Figure 2.

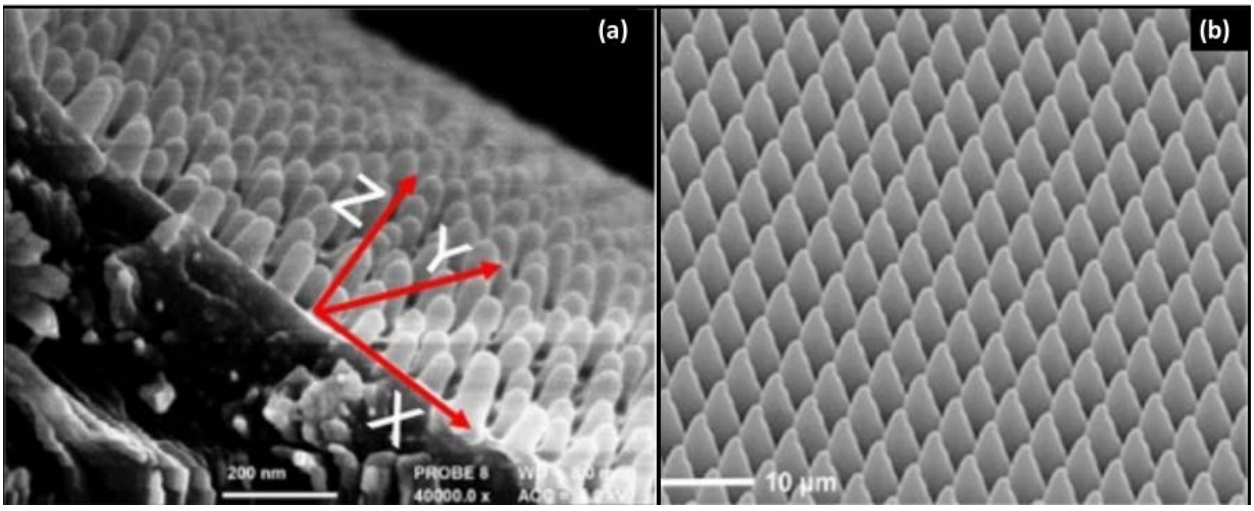

Figure 2: Image examples with high transmissive optical properties of (a) bioinspired microscopic moth-eyed coating and (b) non-bioinspired PDMS stamped micropyramid ARC [22, 27].

Optical pass or block filters, which are generally made of infrared-transparent multilayers, transmit a certain optical spectrum or wavelength through them while rejecting others. For example, a block-band filter is the concept of quarter-wave Bragg reflectors where electromagnetic waves will combine destructively within the device resulting in near perfect reflection, except for at the resonance wavelength, which will eventually escape out of the filter [29]. The shortpass filter transmits wavelengths shorter than the desired wavelength and rejects wavelengths beyond the cut-off. Many shortpass filter concepts have been implemented in the near-infrared wavelengths for optical fiber research [30, 31]. The use of shortpass filters are most notably within color cameras where they attenuate the NIR photons so that the spectral transmittance of color filters can be better matched to the human eye because solar radiation has

significant impact in the NIR wavelengths [32]. Like a distributed Bragg reflector (DBR), a bandpass filter transmits only a portion of the specified spectrum and rejects all others. Interestingly, many of the material specifications and designs are kept as proprietary information within the industry. Generally, bandpass filters combine multiple short- and long-pass filters into an optically thick lens of complex design and processing [33-37]. Longpass filters are used in many different applications. For example, the optical properties are being optimized to have tunable transparency with a new polymeric filter that has various applications such as optical power limiters and protective layers for visible transparency windows [38]. Electrochromic windows are being commercially developed to reduce cooling loads, heating loads, and lighting energy due to their dynamic tintable smart windows [39]. Dichroic mirrors are being developed to achieve ultra-broadband operation that has low insertion loss and octave-wide simulated bandwidths [40]. In addition, various medical imaging devices that operate in the infrared wavelengths are being developed [39-41]. High-precision longpass filters are developed to integrate with miniaturized spectrophotometers, which are commonly found in nano/micro-aperture applications [41].

1.3 Objective

This thesis is aimed at developing a gradient-indexed metamaterial IR detector that can enhance image quality, photo-responsivity, and reduce the need for thermal control devices by remaining a compact profile [42, 43]. The quasioptical metamaterial IR detector that will be analyzed will comprise of three separate components including an anti-reflection coating (ARC), a multi-layer longpass filter, and a micro-pillar focal plane array. The ARC will cover today's various technologies, and how the overall design was inspired through natural design cues. The optical performance of various IR dielectric and semi-dielectric material compositions, such as

low refractive index material potassium bromide (KBr) and polyvinyl chloride (PVC), and high refractive index material optical silicon (Si), will be studied. This analysis is aimed at determining what is the optimal geometric make-up (pyramidal, parabolic, and inverse parabolic), and whether altering the grating's blazing angle has any predominant effects. A 2D RCWA method is used to obtain the transmissive, reflective, and absorption spectral properties, and it has been used in various other studies and demonstrated against an in-house developed 3D RCWA that exceeds the computational performance of previous metasurface studies [44-47]. To better illustrate the transmission and absorption effects around the grating, electric field waveplots were developed to characterize how the grating's shape impacts the electric field.

A gradient-index multilayer longpass filter is tested against layer parameters and minimum deposited layer thickness with sharp transitions from reflection to transmission. The broad highpass filter of alternating dielectric layers are stacked onto the substrate and begins with a low-index period which gradually shifts to a higher-index period as light exits the filter. By alternating quarter-wave layers of KBr and Si, the multilayer is analyzed through plotting normal reflectivity versus wavelength. The development of the multilayer longpass filter allows for near perfect transmission along the cut-off wavelengths before traveling to the planar micropillar metalens.

The purpose of a metalens light focusing photodetector is to enhance the signal-to-noise ratio of the focal plane array, and to replace bulky optical components. Cooling is one of the major limitations for many photodetectors, and a compact design can allow for an absence of active cryogenic cooling methods. Without the proper cooling, there will be a decrease in signal-to-noise ratio as well as a high presence of dark current. This study will dwell into designing a planar micropillar metalens using a graded diameter micropillar with radially varying effective

index of refraction flat disk lens for light concentration. The CdTe substrate will be sandwiched between the MCT detector and metalens plane, and the micropillars will be made of a dielectric with a refractive index greater than that of the photodetector. While the FDTD model used to build and simulate the effects of light concentration has on the photodetector, an extensive look into fabrication of these micropillars will not be explored. However, a brief overview of different fabrication methods and potential new approaches for the metasurface ARC's will be discussed. This simulation does not account for the imperfections in either the ARC grating geometry or the graded diameter micropillars, and the results are merely a proof of concept. Future research on current manufacturing capabilities and sophisticated fabrication techniques are needed to achieve the specific design criteria described in this study.

CHAPTER 2

METHODOLOGY

2.1 Overview

This section explores the governing equations and nomenclature used in for developing the modeling and simulation of the gradient-index metamaterial infrared detector. The grating metasurface will be analyzed through the choices of optical constants through the selection of different high and low index of refraction material. By using the dielectric function, the refractive index can be derived to develop the desired optical characteristic based on the refractive index n and the extinction coefficient κ, which will be further explored in the following sections.

To better understand how the material selection and grating's shape effects the performance of the metasurface, a 2D Rigorous Coupled-Wave Analysis (RCWA) is used to analyze the electric and magnetic fields and how they correlate to the overall reflection and transmission of the ARC. Furthermore, development of the longpass filter was introduced using the Fresnel reflection coefficient transfer matrix method (TMM), which analyzes the propagation of the electromagnetic waves at an interface between two media and through a semi-infinite media.

The gradient-index of refraction (GRIN) metalens will be modeled and simulated using a Finite-Difference Time-Domain (FDTD) method using the ANSYS Lumerical computer software. FDTD is a numerical method for solving differential equation by converting them into a set of linear algebraic equations, which is a powerful numerical method for modeling electromagnetic wave propagation [29]. In later sections, the electromagnetic wave field plots will show how the designed metalens will focus collimated light at a targeted wavelength on the

small micro-pillared photodetector. Lastly, how the micro-pillared metalens on a focal plane array is designed using the GRIN system will be further explored. By radially decreasing the effective refractive index from the optical axis, the microlens spot focusing is achieved.

2.2 Dielectric Function

Across the wavelength region of interest for this metasurface grating, the refractive index is derived from the complex dielectric function ε, which is satisfied by

$$\varepsilon = (n + i\kappa)^2 \qquad \text{(Eq. 1)}$$

where n is the refractive index and κ is the extinction coefficient. Although neither of them is constant over a large wavelength for real materials, the refractive index and extinction coefficients can also be referred to as optical constants [29]. The extinction coefficient measures the damping of the electromagnetic field through the absorption of free electrons and the dipole oscillation of bound electrons [48]. The refractive index and extinction coefficients between the wavelength range of 5 to 15 μm are seen below in Figure 3.

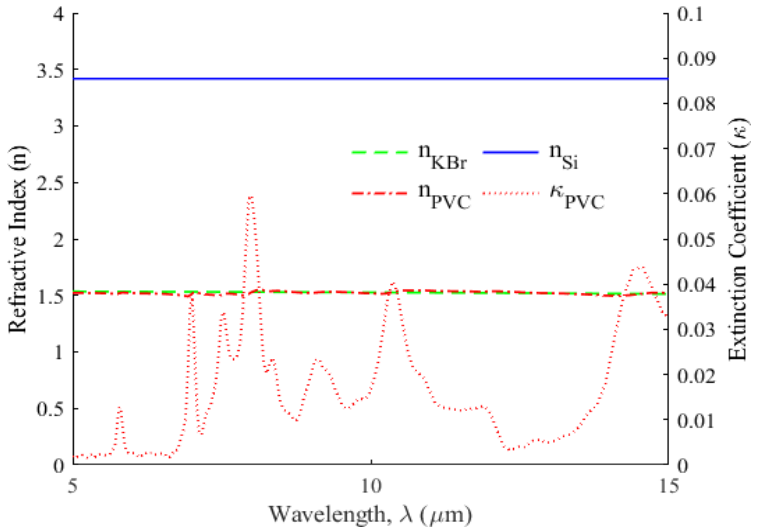

Figure 3: Refractive indices and extinction coefficients within the 5 to 15 μm wavelength are shown on the left and right y-axis, respectfully. The only nonzero extinction coefficient is that of PVC.

The metasurface grating's optical materials used within this study include optical-grade silicon (Si), potassium bromide (KBr), and polyvinylchloride (PVC). Optical-grade silicon was modeled to be at room temperature and selected as the infrared-transparent wafer substrate because of its high-index of refraction $n = 3.42$ with no extinction coefficient. KBr and PVC is used for the ARC's grating surface due to their low index of refractions of $n \approx 1.5$. While KBr had no extinction coefficient, PVC has a nonzero extinction coefficient of $\kappa < 0.1$. While PVC does have a nonzero extinction coefficient, it was chosen due to the possibility of surface micromachining, which would provide for large-scale manufacturing capabilities. Both KBr and PVC were taken from empirical data [49, 50]. The Reststrahlen lattice absorption for KBr is beyond the 70 μm, which is outside the Reststrahlen band and the interest of this study [51]. The Reststrahlen effects is the phenomenon in which a there is a high level of reflectance in a dielectric material that is otherwise transparent [29].

2.3 Rigorous Coupled-Wave Analysis (RCWA) for 2D Gratings

The RCWA method is a well-known numerical method for calculating the optical properties of a gratings geometry with sufficient accuracy by using a Fourier-space method [29]. The Fourier-space method treats the electric and magnetic fields as a sum of spatial harmonics (diffraction orders) [51]. Within this study, a 2D homogeneous and isotropic-sectioned RCWA method was developed to better understand how the material and geometry effected the gratings performance [44-47]. This method uses the Bloch-Floquet condition by describing tangential component of the wavevector of each diffractive wave [47]. The dielectric function of any layer can be expanded by the Fourier series due to the periodic structure of the grating. The spatial harmonics are taken to be sufficiently large so that the far-field diffraction effects in both the electric and magnetic fields can be obtained. However, it is important to note that by making

them too large that it will make the computations too extensive, which will lead to more time and money spent.

Because the ARC grating layer is periodic, the permittivity and permeability for the layers need to be Fourier-expanded, which will yield the spatial diffraction harmonics of the electromagnetic waves. This is completed combining the wavevector components for each layer through numerically solving a Fourier-space version of Maxwell's equations. Because the RCWA method is dependent on the number of spatial harmonics that are used, the accuracy of the reflectance was based on how the solution converged. Neither the Gibbs phenomenon nor Wood's anomalies were observed because the dielectric contrast is insignificant compared to the grid resolution and the surface plasmon polaritons are only excited on metallic layers, respectfully [52, 53]. Because this method is known for providing and accurate analysis of the periodic structures, multiple cases of varying geometry were studied for both the reflectance of KBr and the absorption of PVC.

2.4 Transfer Matrix Method for Multilayers

The Transfer Matrix Method (TMM) analyzes the propagation of electromagnetic waves at an interface between two media and through a semi-infinite media as they pertain to the reflectivity and transmissivity of a multilayer structure. This multilayer was modeled to be semi-infinite, homogeneous, and anisotropic and for the use of uniaxial multilayered structures or heterostructures [29]. The incident wave is taken to be at normal incidence, which equates to the x and y component wavevectors relating to k_x and k_y being zero. The transverse wavevector component for all any of the layers, j, can be expressed as $k_{j,z} = k_0 n_j$. By alternating between high and low-index material and setting the thickness of each layer to be quarter-wavelength, a traditional block filter can be developed. The quarter-wavelength thickness can be described as

$d_{min} = \lambda_c/4n_j$ where λ_c is the cut-off wavelength. The cut-off wavelength is defined as the chosen wavelength in which the transmittance is decreased to 50%. The layer under the ARC grating starts as a low index layer and is further divided into alternating index layers. As the periods progress deeper into the multilayer, the alternating index layers have a gradually increasing filling ration denoted by

$$\phi = \frac{pd_{min}}{\Lambda} \quad \text{(Eq. 2)}$$

where *p* describes the low and high-index period number, rounded to the nearest integer, into the multilayer from 1 to Λ/d_{min}.

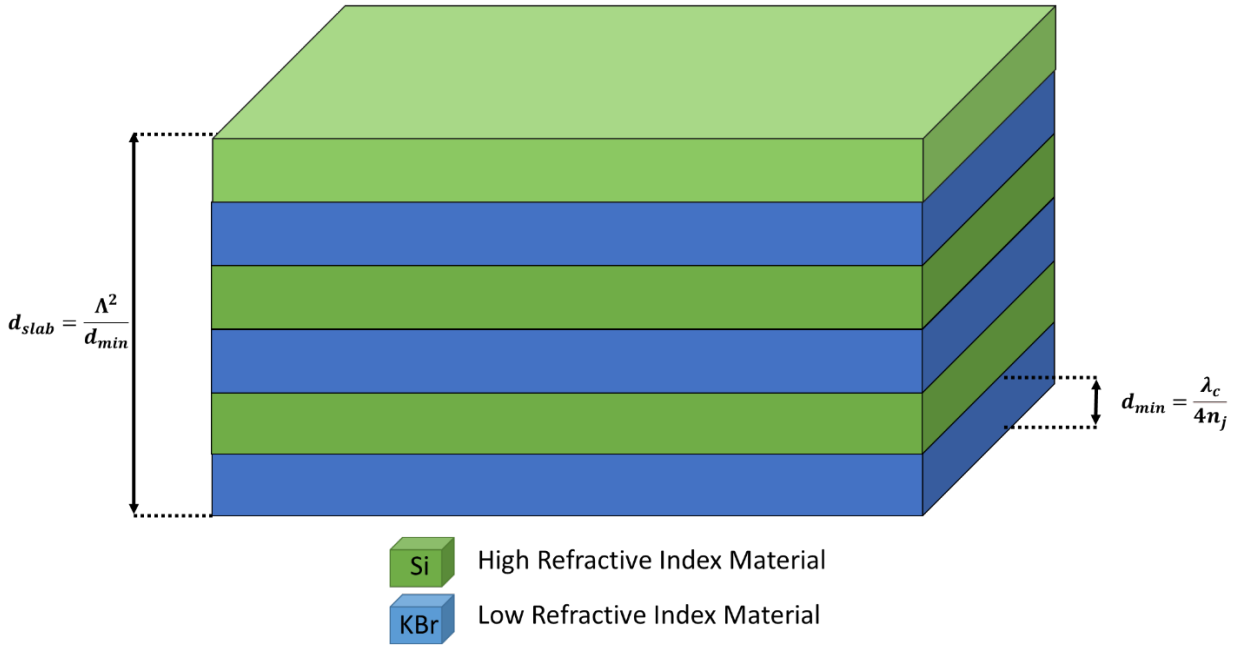

Figure 4: **Illustration of a multilayer quarter wave stack of alternating material compositions of high refractive index of KBr and low refractive index of Si.**

While the reflectivity and transmissivity of multilayers can be controlled quite accurately with various thin-film deposition techniques, different materials have different limitations, such as physical vapor deposition (PVD) versus chemical vapor deposition [21, 29]. The total slab thickness for the multilayer filter can be expressed as

$$d_{slab} = \frac{\Lambda^2}{d_{min}} \quad \text{(Eq. 3)}$$

For TMM, the electric and magnetic field amplitudes at the incident surface of the device are related to the outgoing substrate medium, denoted by *N* [11]. *N* is the total number of layers and can be expressed by $N = 2\Lambda/d_{min}$. The electric and magnetic field amplitudes at the incident surface can be expressed by

$$\begin{pmatrix} A_1 \\ B_1 \end{pmatrix} = \prod_{j=1}^{N-1} \frac{1}{t_{j,j+1}} \begin{pmatrix} e^{-ik_{j,z}d_j} & 0 \\ 0 & e^{-ik_{j,z}d_j} \end{pmatrix} \begin{pmatrix} 1 & r_{j,j+1} \\ r_{j,j+1} & 1 \end{pmatrix} \begin{pmatrix} A_N \\ B_N \end{pmatrix} \quad \text{(Eq. 4)}$$

The Fresnel reflection and transmission coefficients at the interface are denoted as $r_{j,j+1}$ and $t_{j,j+1}$ between the consecutive layers *j* and *j*+1, respectfully. Furthermore, the product of Eq. (4), referenced by **M**, leads to the reflectance and transmittance of the device calculated by the following:

$$R_\lambda = \left|\frac{\mathbf{M}_{21}}{\mathbf{M}_{11}}\right|^2, \qquad T_\lambda = Re\left[\frac{\varepsilon_{sup}}{\varepsilon_{sub}} \cdot \frac{k_{z,sub}}{k_{z,sup}}\right] \left|\frac{1}{\mathbf{M}_{11}}\right|^2 \quad \text{(Eq. 5)}$$

Near-field surface plasmon coupling doesn't need to be accounted for when creating a multilayer filter with a zero-extinction coefficient with alternating high- and low-index dielectric materials [54]. By using this method, the reflectivity and the transmissivity of the multilayer can be easily calculated and designed.

2.5 Finite-Difference Time-Domain (FDTD) Method for Image Focusing

By using a finite-difference time domain (FDTD) method to simulate the metalens, the electric field densities are analyzed to show the results of the device's performance. The FDTD method is ideal for full-wave simulation modeling as it provides an accurate representation of its performance, but it is generally hindered by a lengthy computational time for larger diameter metalenses. However, an application of hardware-accelerated 3D FDTD solver to

electromagnetic acceleration simulation provides a path forward to full-wave modeling and optimization for large-scale metalenses within a reasonable time frame by employing a simpler full-domain modeler that retains the full accuracy solution of Maxwell's equations [55]. Furthermore, the approach in this study uses an FDTD solver through ANSYS Lumerical computer software, which uses state-of-the-art methods for solving Maxwell's equations.

The FDTD is a numerical method for modeling electromagnetic wave propagations and scattering in broad frequency regions for both very large and very small geometric structures [29]. Specifically, it provides a solution for both time and space, which can be used to determine performance characteristics for the microlens spot focusing. The original FDTD idea inspired by Kane Yee, and often described as the Yee cell. It is assumed that the *E* and *H* fields are surrounding a cell whose origin is at the location *i*, *j*, and *k*. The electric field ($\vec{E}$) and magnetic field ($\vec{H}$) is defined as

$$\vec{E}(\boldsymbol{r}, t) = E_0 \cos(\omega t - \boldsymbol{k} \cdot \boldsymbol{r} + \phi_0) \quad \text{(Eq. 6)}$$

$$\vec{H}(\boldsymbol{r}, t) = H_0 \cos(\omega t - \boldsymbol{k} \cdot \boldsymbol{r} + \phi_0) \quad \text{(Eq. 7)}$$

where E_0 and H_0 are the electric field and magnetic field amplitude, respectfully, ω is the angular frequency, *t* is time, $\boldsymbol{k}$ is the wave vector, **r** = (x, y, z) is the position vector, and ϕ_0 is the phase angle. Every *E* field is located ½ a cell's width from the origin in the direction of its orientation while every *H* field is offset ½ a cell's width in each direction except that of the orientation [56]. The governing equations that are used within the FDTD solver, ANSYS Lumerical, are based on Maxwell's curl equations for non-magnetic materials, and are described by

$$\frac{\partial \vec{D}}{\partial t} = \nabla \times \vec{H} \quad \text{(Eq. 8)}$$

$$\vec{D}(\omega) = \varepsilon_0 \varepsilon_r(\omega) \vec{E}(\omega) \quad \text{(Eq. 9)}$$

$$\frac{\partial \vec{H}}{\partial t} = -\frac{1}{\mu_0}\nabla \times \vec{E} \quad \text{(Eq. 10)}$$

where the displacement, magnetic, and electric fields are denoted by *D*, *H*, and *E*, respectfully. Furthermore, the complex relative dielectric constant $\varepsilon_r(\omega)$, which can also be related to the refractive index $n^2 = \varepsilon_r(\omega)$. For this 3D FDTD simulation the Maxwell equations could be broken down into 6 components including Ex, Ey, Ez and Hx, Hy, and Hz Maxwell's equations could be split into two independent series of equations for transverse electric (TE) and transverse magnetic (TM) equations [56]. These six scalar normalized value equations are as follows:

$$\frac{\partial D_x}{\partial t} = \frac{1}{\sqrt{\varepsilon_0 \mu_0}}\left(\frac{\partial H_z}{\partial y} - \frac{\partial H_y}{\partial z}\right) \quad \text{(Eq. 11a)}$$

$$\frac{\partial D_y}{\partial t} = \frac{1}{\sqrt{\varepsilon_0 \mu_0}}\left(\frac{\partial H_x}{\partial z} - \frac{\partial H_z}{\partial x}\right) \quad \text{(Eq. 11b)}$$

$$\frac{\partial D_z}{\partial t} = \frac{1}{\sqrt{\varepsilon_0 \mu_0}}\left(\frac{\partial H_y}{\partial x} - \frac{\partial H_x}{\partial y}\right) \quad \text{(Eq. 11c)}$$

$$\frac{\partial H_x}{\partial t} = \frac{1}{\sqrt{\varepsilon_0 \mu_0}}\left(\frac{\partial E_y}{\partial z} - \frac{\partial E_y}{\partial z}\right) \quad \text{(Eq. 11d)}$$

$$\frac{\partial H_y}{\partial t} = \frac{1}{\sqrt{\varepsilon_0 \mu_0}}\left(\frac{\partial E_z}{\partial x} - \frac{\partial E_x}{\partial z}\right) \quad \text{(Eq. 11e)}$$

$$\frac{\partial H_z}{\partial t} = \frac{1}{\sqrt{\varepsilon_0 \mu_0}}\left(\frac{\partial E_x}{\partial y} - \frac{\partial E_y}{\partial x}\right) \quad \text{(Eq. 11f)}$$

By using the finite difference numerical differentiation, the derivatives can be approximated by breaking them down into different sets of linear algebraic equations using a spatial mesh (or grid) scheme in relation to their *i*, *j*, and *k* location [29]. Using the computer analysis tool, ANSYS Lumerical, different combinations of materials and geometric designs of structures can be quickly modeled to provide interesting data such as electric field density plots for light focusing, and focal plane density plots to determine collection efficiency.

CHAPTER 3

METAMATERIAL INFRARED DETECTOR DISCUSSION

3.1 Anti-Reflection Coatings Analysis

Through the use of the 2D RCWA method, the micropatterned dielectric metasurface is analyzed at normal incidence, and considered to be in vacuum free-space. The analysis pertaining to this section will include examining how varying the geometric grating of the ARC will impact the transmissivity, reflectivity, and the electric field densities. In section 3.1.1, the KBr and PVC metasurface materials will be investigated to show how varying the blazing angle (α) and the cross-sectional structure impacts their reflectivity and absorption characteristics, respectively.

3.1.1 2D Shape Factors

In this section, the 2D RCWA method was used to analyze how altering the metasurface periodic grating and cross-sectional geometrical shape will impact the reflectivity of KBr and the absorption of PVC. Due to the previously observed index matching in Figure 3, the reflection of PVC will not be analyzed in detail because it would be nearly identical to KBr.

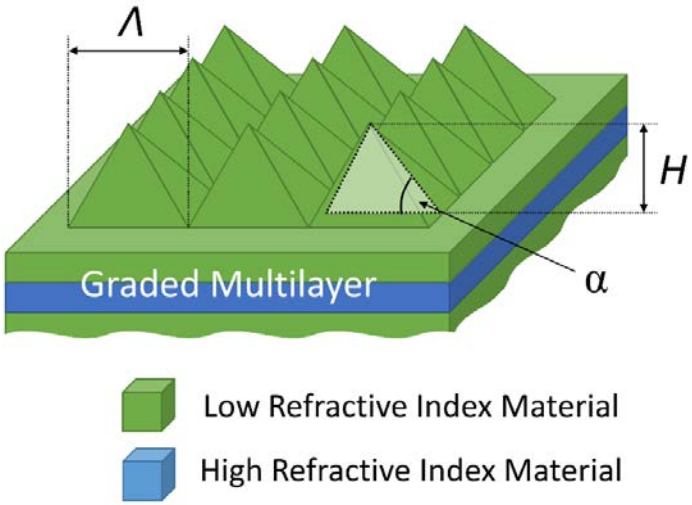

Figure 5: **Illustration of the metasurface periodic grating ARC**

The first analysis was conducted by keeping a consistent pyramidal geometric structure while only varying the blazing angle (α). In Fig. 6(a), the blazing angle was varied in increments of 20 degrees with a range of 25 to 65 degrees to determine the effects that it has on the reflection and absorption characteristics for a pyramidal-shaped grating.

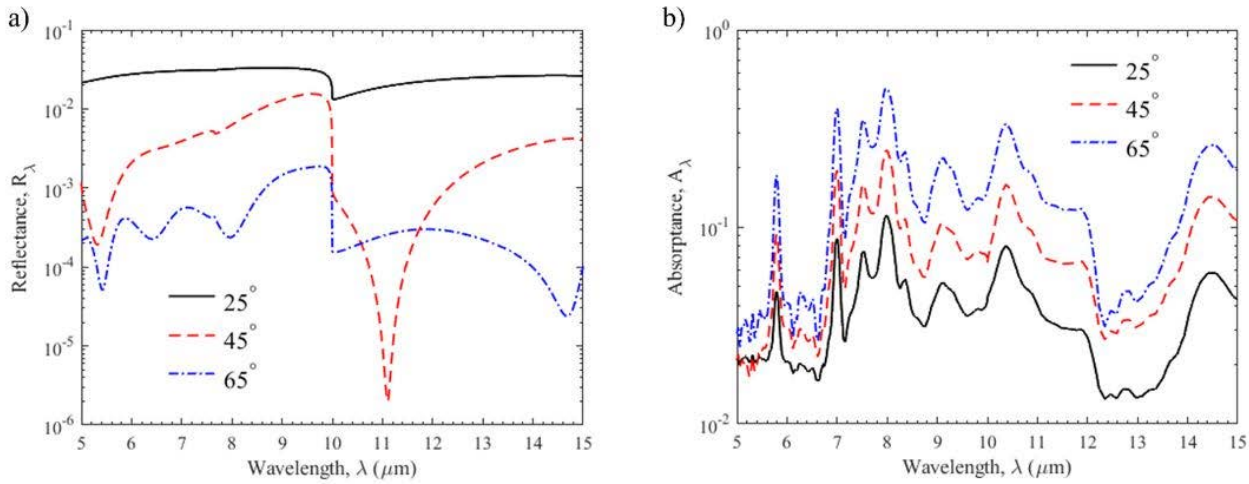

Figure 6: **Reflectance and absorption in transverse magnetic polarization with varying blazing angles of (a) KBr metasurface and (b) PVC. Wavelength of study are both within 5 to 15 μm.**

The grating had a fixed period of Λ = 10 μm and was used in conjunction with the blazing angle (α) to calculate the total thickness (*H*). The total thickness (or height) of the grating array is defined as

$$H = \frac{\Lambda \tan \alpha}{2} \qquad \text{(Eq. 12)}$$

where α is the blazing angle. By inputting the wavevectors and thicknesses, the width-to-period filling ratio for the discretized grating form can be calculated. The width-to-period filling ration for each layer is defined by as

$$\frac{W_j}{\Lambda} = 1 - \frac{j d_{min}}{H} \qquad \text{(Eq. 13)}$$

where W_j is the width of layer j. Each developed individual geometry uses these parameters for each 2D shape factor for the grating's design. Once the grating's design is established, the 2D RCWA method was utilized.

Due to the complexity and performance dependency of these gratings, too sharp- and too sharp-angled gratings may not be of interest due to fabrication feasibility. While the metasurface material of PVC was considered due to its manufacturability, an in-depth look into fabrication is yet to be explored for these various geometric shapes and the results are purely theoretical. The reflectance maxima for KBr are 3.31×10^{-2}, which closely resembles to the normal reflection of flat KBr calculated by $R = (n_{KBr} - 1)^2/(n_{KBr} + 1)^2 \approx 0.04$. Alternatively, the global reflectance minima are 1.97×10^{-6}. Interestingly, the minima are generally situated near the wavelength, which corresponds to the period of the grating. The 25-deg blazing angle had minimal impact over flat KBr, which only showed a reduction as it corresponded at the period wavelength. From Table 1, the performance wavelength bands for various blazing angles can be seen to allow for a better interpretation of the data. However, grating with a 45-deg blazing angle configuration for quasioptical coupling at the targeted wavelength could be considered the "Goldilocks" configuration.

Table 1: **Reflectance and absorption performance characteristics in transverse magnetic polarization with varying blazing angles of (a) KBr metasurface and (b) PVC. Wavelength of study are both within 5 to 15 μm.**

Varying Blazing Angles	**Optimal Performance Wavelength (**μm)	**High Performance Band (**μm)	**Low Performance Band (**μm)
Reflectance of KBr	11.1	10-12	9-10
Absorption of PVC	12.35	5-7 & 12-14	7-12

From Fig. 6(b), the PVC gratings absorption can be seen with varying blazing angles like that of the KBr grating. Similarly, the absorption characteristics followed the spectral peaks and valleys, but shallower blazing angles showed decreasing magnitudes. The 25-deg blazing angle had the lowest absorption over all the other measure angles. However, the 45-deg and 65-deg blazing angles also showed low levels of absorption, which in this case would be considered suitable for this application. From Table 1, the highest performance wavelength bands are shown

and expected based on the previously examined low extinction coefficients shown in Fig. 3. Furthermore, this proves that there PVC as an easily micromachined ARC for specific wavelength applications is a viable option for high metasurface volumes with sharp angled gratings.

To expand upon the analysis that was already completed above, an additional analysis was conducted to determine which geometrical shaped grating would provide the highest performance in low reflectivity when compared to that of a pyramidal shaped grating. In Fig. 7(a), three KBr grating shapes were compared: pyramidal, parabolic, and inverse parabolic. The parabolic and inverse parabolic cases did not vary as much over the specified wavelength when compared to that of the pyramidal case. However, all three cases showed nearly ~100% transmittance, which proves that KBr is a sufficient material composition for the entire spectrum of the analysis. The reflectivity showed a sharp decline just above the at-period wavelength for the pyramidal grating design because linearity of the effective index of the graded layers. Furthermore, it can be observed that the parabolic grating slightly improves over the inverse parabolic case due to the easing of the effective index, which further strengthens that a periodic "needle" microstructure is unfavorable over the "mound" microstructure.

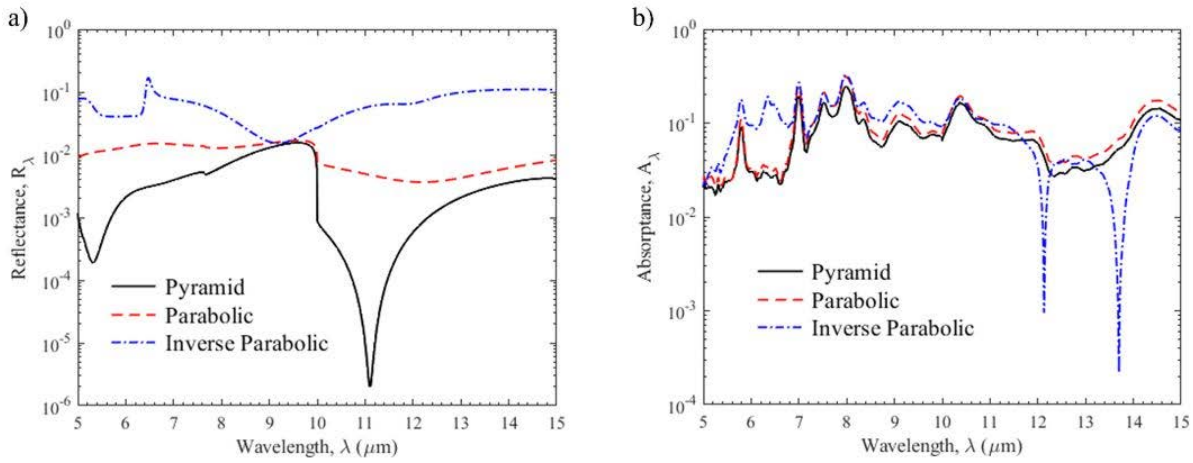

Figure 7: **Reflectance and absorptance in TM polarization with varying geometric shape variations: pyramid (default), parabolic, inverse parabolic, metasurface made of (a) KBr and (b) PVC.**

By varying the geometry of the PVC metasurface, it was observed that the absorptance showed little change over the entire wavelength spectrum due to the fixed grating heights (*H*). However, there were two minima located at 12.13 and 13.70 μm for the inverse parabolic shape. The reason for the sharp spikes isn't exactly known, but there is an inference that it is due to some computational singularities that were generated from trying to calculate the sharp tip of the "needle" microstructure. From Table 2, the performance of varying the geometric shape of the ARC's grating shows little effect across the entire wavelength spectrum in this analysis, which is like the results seen in Fig. 6(b) by altering the blazing angle.

Table 2: Reflectance and absorptance performance in TM polarization with varying geometric shape variations: pyramid (default), parabolic, inverse parabolic, metasurface made of (a) KBr and (b) PVC.

Varying The Geometric Shape	Shape	Optimal Performance Wavelength (μm)	High Performance Band (μm)	Low Performance Band (μm)
Reflectance of KBr	Pyramid	11.10	10-12	6-10 12-15
	Parabolic	12.19	10-15	5-10
	Inverse Parabolic	9.19	9-10	5-9 10-15
Absorption of PVC	Pyramid	5.25	5-5.7 5.85- 6.89 12.13-13.70	5.7-5.85 6.89-12.13 13.70-15
	Parabolic	5.36	5-5.7 5.85- 6.89 12.13-13.70	5.7-5.85 6.89-12.13 13.70-15
	Inverse Parabolic	5.06	5-5.7 12.13-13.70	5.7-12.13 13.70-15

The analysis ratio of KBr transmission and PVC absorption showed that the sharp inclination of the 45-deg blazing angle pyramidal shaped ARC was optimal for reducing the amount of reflectance as opposed to shallower and steeper angles. Additionally, the parabolic and inverse parabolic shapes had similar effects. While other complex periodic grating shapes may offer better antireflection characteristics, it is important to understand that extending to a

second-order progression of effective refractive index of layers does not improve over the linearly expanded cross-sectioned triangular gratings.

Furthermore, the absorptance of the PVC metasurface gratings results showed that a blazing angle of 25-deg would provide the highest performance characteristics overall by providing the lowest levels of absorption. The 45-deg blazing angle would also be a favorable option especially for low-κ wavelength windows. Overall, the PVC pyramidal grating structure would be the optimal choice due to its manufacturability over other geometrical shapes, but any of the shapes studied would suffice due to low impact that shape plays on the absorption characteristics.

3.1.2 Electric Field Densities of the ARC

The cross-sectional electric field plots at TM polarization for all three cases of geometrical shaped gratings were generated at $\lambda = 10\ \mu m$ and can be seen in Fig. 8. Undisturbed electric field lines in the incident vacuum medium generally indicates high transmission. The pyramidal- and parabolic-shaped gratings showed electric field concentrations in the upper portions of the grating as well as in the valleys. In the case of the inverse parabolic-shaped grating, the electric filed concentrations were lower in the valleys, but had higher levels of concentration in the peaks of the grating.

The pyramidal- and parabolic-shaped gratings electric field's magnitude decreased as the electromagnetic waves entered the grating, which can be seen as the darker regions become more prominent. However, the opposite is true regarding the inverse parabolic shaped grating. Fig. 8(c) shows that the electric field concentrations increase immediately after the electromagnetic waves enter the ARC. While all three cases have varying electric field concentrations within the geometrical shaped gratings, both the pyramidal- and parabolic-shaped gratings have lower

levels of concentration when compared to the inverse parabolic-shaped grating. Furthermore, it is shown that the pyramidal-shaped grating has the lowest levels of electric field concentrations at the ARC's transition. The inverse parabolic-shaped grating has a consistent electric filed concentration through its entire depth of the ARC.

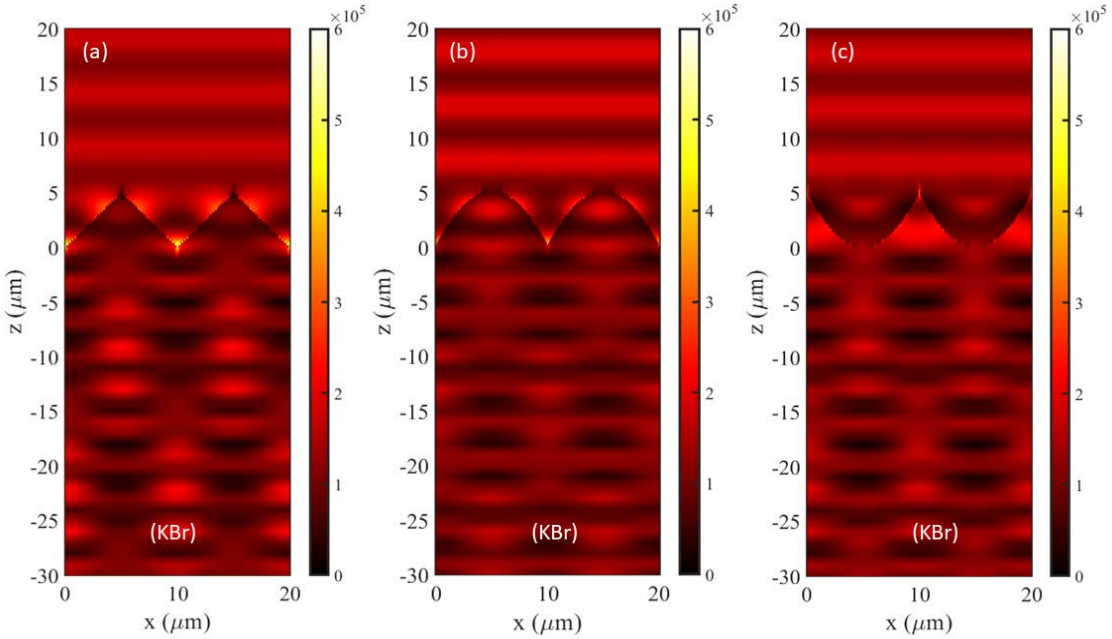

Figure 8: Cross-sectional metasurface grating electric field density plots at TM polarization using 2D RCWA for (a) pyramid, (b) parabolic, (c) inverse parabolic made of KBr at a 10 µm wavelength.

The device proposed in this analysis is theoretical in nature, and further simulation and experimentation is required for real-world application due to the imperfections that could arise during the fabrication process. Furthermore, particular attention must be made regarding the minimum layer thickness requirement to avoid wide wavelength drop-off when designing and fabricating the longpass filter in this study. Similarly, the requirements for the quarter-wave layer thickness requirement through deposition strategies must also be considered.

3.2 Gradient-Index Dielectric Multilayer for Infrared Longpass Filtering

In Fig. 9, various designed cutoff wavelengths are shown regarding the reflection bands

of a gradient material KBr/Si longpass filter. The first layer (KBr) has a minimum layer thickness of $d_{min} = 10\ nm$. To ensure that each layer is quarterwave for KBr and Si, the period thicknesses are chosen as $d_j = 1.7, 2.4, and\ 3.1\ \mu m$ for the respective three cases that are presented. Minimum reflection occurs just beyond the designed cutoff wavelengths for quarter-wave designs. For these periodic thicknesses, steep drop-offs in reflection can be seen near the cutoff wavelengths due to the combined effects of the constructive interference and the partially reflected waves at each interface. The gradient multilayer medium begins to look like an effective medium when above the period size because the interference effects do not occur [54]. At $R_\lambda \approx 0.995$ below the cutoff wavelength, the reflection remains nearly constant. However, at $R_\lambda << 0.01$ the reflection has a sharp decline until it reaches stability at $R_\lambda \approx 10^{-4}$, which is far beyond the cutoff wavelength.

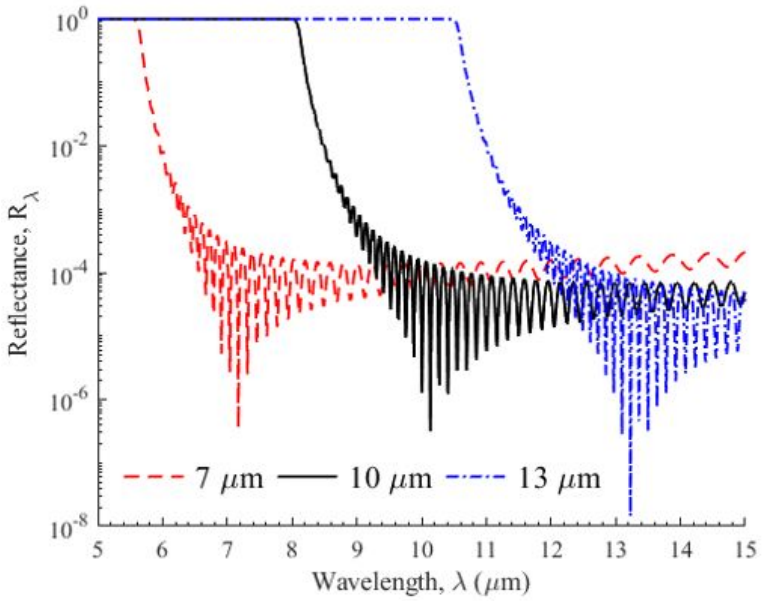

Figure 9: **Reflectance bands KBr/Si Longpass filter with cutoff wavelengths at 7, 10, and 13 µm with a minimum layer thickness of $d_{min} = 10\ nm$.**

From Fig. 10, the relationship between d_{min} and the drop-off step width of the longpass filter can be seen. The drop-off step width of the filter is described as the difference between the

beginning and end wavelengths. The corresponding beginning and end wavelengths are $R_\lambda = 0.995$ and $R_\lambda = 0.005$, respectively. When looking at the at the data points in Fig. 10, there is a semi-linear trend between the d_{min} and the drop-off step width. By stepping into the multilayer period-by-period, the filling ratio ϕ increases, and the smaller the drop-off step width will be. However, this will require more layers, so d_{slab} will increase proportionally to d_{min}. For example, consider both to have a $\lambda_c = 10\ \mu m$. With a $d_{min} = 10\ nm$, the d_{slab} would equate to having a 140.4 μm thick slab. However, a $d_{min} = 100\ nm$ would equate to a d_{slab} having a 13.2 μm thick slab. In some instances where d_{min} becomes close to zero, it could be expected that the drop off would be perfectly steep at the design cut-off wavelength.

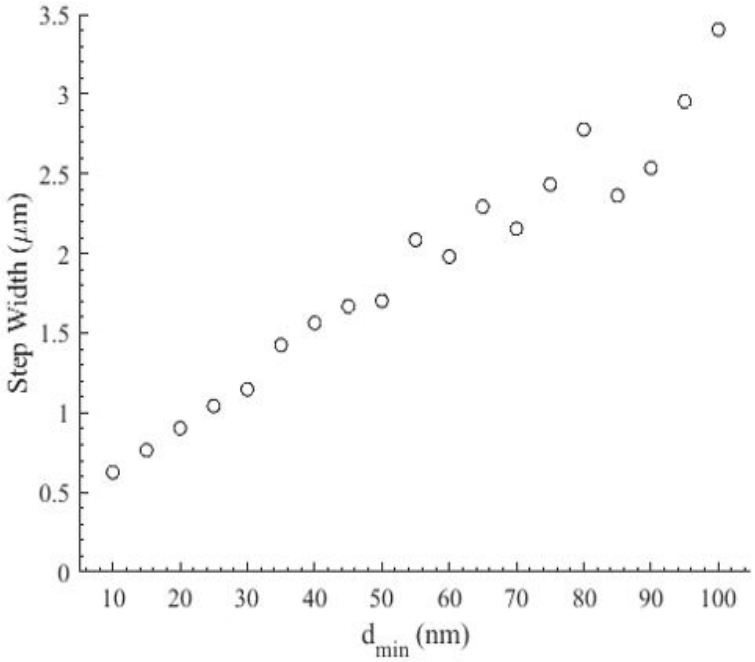

Figure 10: **Drop-off step with dependence on d_{min} of a longpass filter with $\lambda_c = 10\ nm$, and a drop-off step width between $R_\lambda = 0.995$ and $R_\lambda = 0.005$.**

3.3 Gradient-Index Metalens System

This state of the art metalens design models the concept of a GRIN lens, which is designed in such a way that the index of refraction gradually decreases radially from the optical

axis [57]. To achieve the radially decreasing index of refraction, a series of cylindrical micropillars were arranged based on their filling ratio and their distance to one another. Thus, achieving an optimized radial refractive index grating that will allow for a smaller focus to aperture ratio. The smaller the focus to aperture ratio, the greater concentration of light—which provides better image quality due to there being less diffraction effects. In principle, the light will travel slowly through an optically dense region and speed up in less dense regions. As one moves more radially outward from the optical axis, the light will more likely bend allowing for greater light concentrations of photons onto the photodetector.

To model the single-phase achromatic planar lens, the effective refractive index n(r) with a material having an index n_0 can be expressed as

$$n(r) = n_0 + \frac{F - \sqrt{r^2 + F^2}}{t} \quad \text{(Eq. 14)}$$

where r, F, and t represent the radius of the disk, focal length, and uniform height of the micropillars, respectfully [57]. The designed metamaterial metalens was modeled to include two different scenarios to prove how the focal distance and electric field magnitude concentrations behave with the use of PVC and Si based substrates and pillars. Figure 11 below shows an illustration of the first case of a PVC substrate and pillar design and its relation to the utilization of the GRIN system. The two cases revolve around changing the material composition of the metalens substrate between PVC and Si. The constants include a medium made of cadmium telluride (CdTe). Future studies will include using the same set up, but also including a mercury cadmium telluride (MCT) detector and a gold (Au) detector casing depicted below.

For this simulation, key parameters were chosen to provide the greatest accuracy while still taking into consideration the simulation time. A conformal meshing technique was applied to the metalens to ensure that the complexity of the structure with the added interfaces between

the micro-pillars and CdTe medium were taken into consideration. Lumerical's Conformal Mesh Technology (CMT) can achieve the results in 1/10 of the time due to the $(\frac{1}{dx})^4$ dependence for the simulation time on the mesh size and provides submesh sensitivity to changes in geometry [58]. The minimum mesh step size was set to 0.00025 μm and a dt time step of ~0.39 fs. Furthermore, the total simulation time was set to 5000 fs, and the signal vs. time pulselength was ~49.54 fs. Using the Courant number described by

$$\nu = \frac{c\Delta t}{n\Delta x} \quad \text{(Eq. 15)}$$

where c is the speed of light, Δt is the total simulation time, n is the materials index of refraction, and Δx is the min mesh step [59]. When the Courant number is less than or equal to 1, the numerical method is conditionally stable, which agreed with the selected parameters in this simulation. The chosen boundary conditions included symmetric for the x- and y-min, metal for z-max, and phase match layer (PML) for the remaining sides. The PML boundary condition was to simulate the infinite space of the finite computation grid, and the metal was to ensure no absorption of light past the focal point electric field concentration.

From analyzing the two cases of PVC and Si, the focal length (F) varied by ~10 μm with the material composition of Si having the smaller focal length at ~55 μm, and PVC having the greatest focal length at ~65 μm in the z-direction. Through different iterations, the thickness of the CdTe medium was altered so that the MCT detector is in the optimal position to meet the highest electric field concentration at the focal point prior to its inclusion into the design. However, difficulty in obtaining optical properties for MCT led to the exclusion of the detector in this study, but the simulation set-up was found to be important for the reader to understand how the CdTe medium was constructed in relation to the focal length. While also excluded due to MCT optical property difficulty, the Au detector casing would be placed on top of the MCT

detector to minimize any further absorption of light past the MCT detector. Due to these limitations, the upper boundary layer was selected as “metal” to prevent any absorption of light.

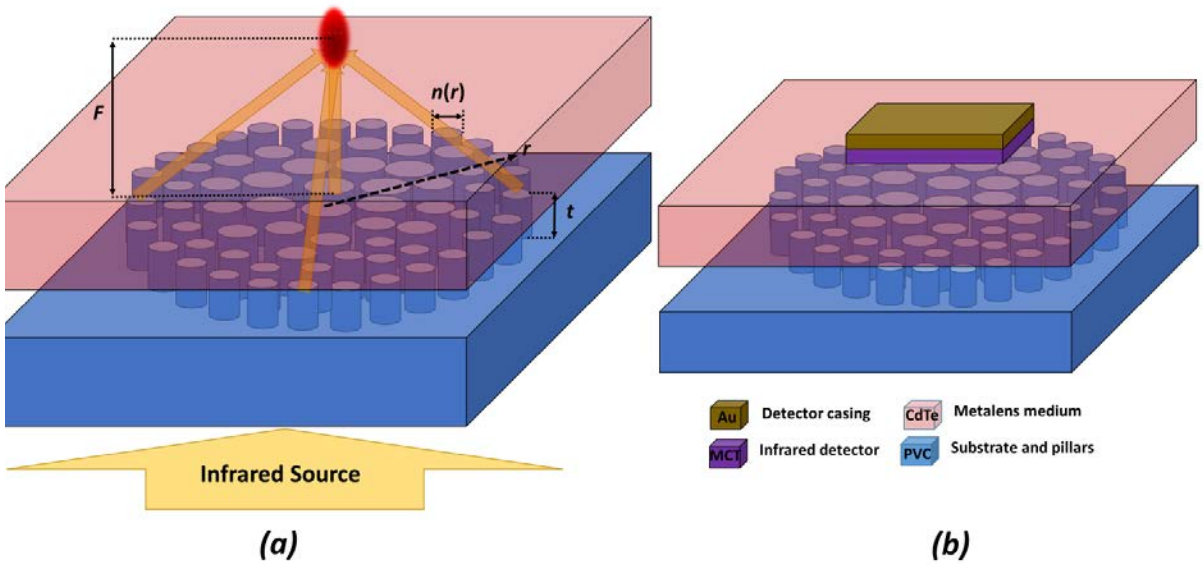

Figure 11: Illustration for the (a) gradient-index metalens focusing concept and how the effective refractive index n(r) varies with increasing radius, and (b) the complete metalens structure.

Figure 12 shows the results from the ANSYS Lumerical’s FDTD analysis on both the metalens material compositions of PVC and Si with and without the use of a CdTe medium as previously shown in Figure 11(a). PVC and Si both obtained the largest focal distance from the metalens with the inclusion of the CdTe medium. However, they also had the smallest electric field concentrations at the focal point. The focal distances for PVC and Si with the CdTe medium are ~65 μm and ~55 μm, respectfully. The electric field magnitude concentration for PVC and Si with the CdTe medium is 0.911 $\frac{V^2}{m^2}$ and 1.69 $\frac{V^2}{m^2}$. Alternately, the focal distances for both PVC and Si are much shorter with the exclusion of the CdTe medium, which can be expected. The focal distances for PVC and Si without the CdTe medium are ~22 μm and ~21 μm, and the electric field magnitude concentrations are 3.95 $\frac{V^2}{m^2}$ and 6.20 $\frac{V^2}{m^2}$, respectfully.

The farfield at the focal point can be seen in Figure 12(a) for all four simulations on both

material compositions. Both cases for PVC and Si farfield at the focal point can be examined by looking at their full width half maximum (FWHM). The electric field magnitude peak of the farfield at the focal point for both PVC and Si are the greatest with the exclusion of the CdTe medium, and their FWHM are ~2.25 μm and ~3.5 μm, respectfully. For the cases with the CdTe medium, PVC and Si had lower electric field magnitude peaks, and their FWHM are ~0.45 μm and ~0.875 μm. Importantly, the inclusion of the CdTe medium allows the light concentration to converge at the focal point proving that this metamaterial metalens concept is practical for reducing the size of the photosensitive area.

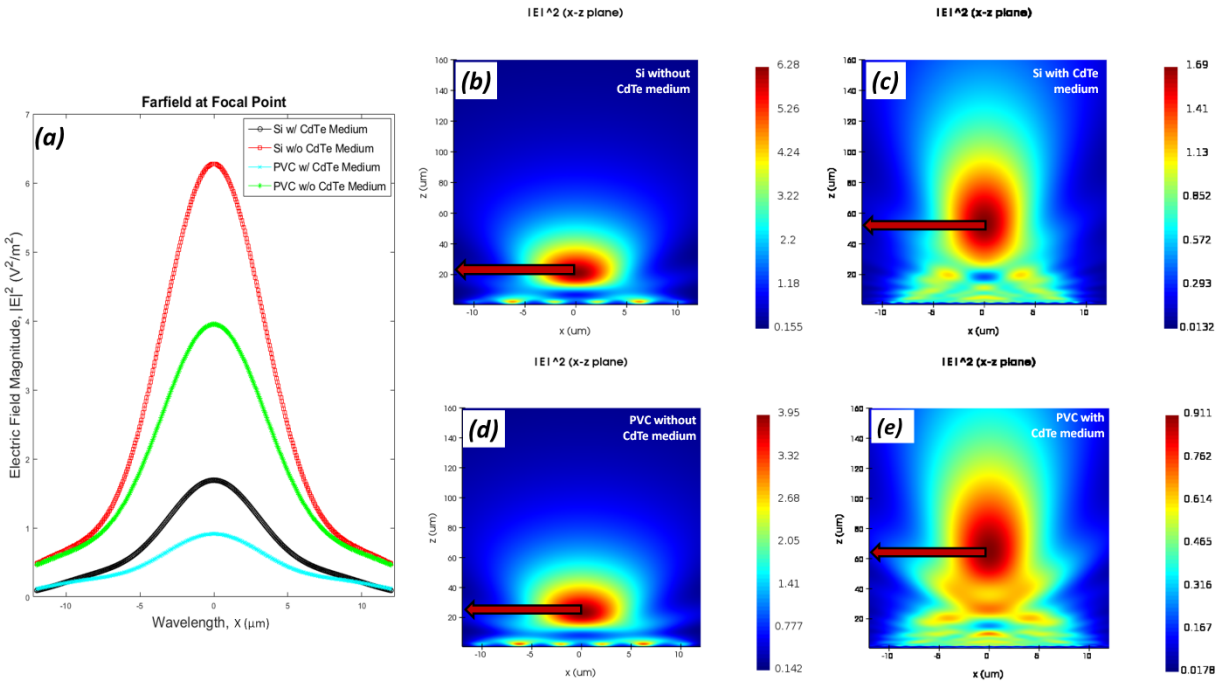

Figure 12: **Metamaterial metalens (a) farfield at focal point for Si and PVC with and without a CdTe medium, and electric field magnitude concentrations for (b) Si without CdTe medium, (c) Si with CdTe medium, (d) PVC without CdTe medium, and (e) PVC with CdTe medium for x vs. z plane.**

While this design and concept presents many new opportunities for advancement for IR detectors, there are still many unknowns and challenges yet to be faced. As technologies advance, new research will also follow. The following concepts will need to be further explored:

(1) experimentation with new material compositions for both ARC and metalens structures with unique optical properties and phase change characteristics, (2) 3D printed metamaterials to drive down cost and increase manufacturability, (3) multi-band detectors, and (4) explore advance manufacturing techniques to obtain complex geometric structures for ARC.

CHAPTER 4

CONCLUSION

In conclusion, a gradient-indexed metamaterial metalens concept has been proposed to combat IR detectors' most common challenges in today's market. The future of IR detection depends on devices becoming compact, lightweight, cost-effective, and able to obtain multi-band detection while not compromising image quality or photo-response time. An anti-reflection periodic grating, longpass IR filter, and a GRIN system metalens was designed and analyzed to increase photo-response time and image quality through increased light concentration of specific wavelengths at a precise focal point. Using the RCWA method, a periodic grating for antireflection with material compositions of KBr and PVC was analyzed to prove their structure's geometric make-up changes the performance of its optical properties. Multilayer band-pass filtering with a material composition stack of KBr/Si was further analyzed to prove that minimum reflection occurs just beyond the designed cut-off wavelength before eventually stabilizing at $R_\lambda \approx 10^{-4}$. A gradient-indexed metalens system was designed and analyzed using a FDTD software tool ANSYS Lumerical to prove that the electric field concentration and focal point distance can be improved through reducing the focus to aperture ratio and altering the material properties of the substrate, pillars, and medium. Through the combination of these three components, a proof of concept has been established to show that near perfect transmission with minimal absorption is possible at targeted wavelengths with certain material compositions and by harnessing a GRIN metalens can increase light concentrations at a specific focal point.

REFERENCES

1. Li, K., et al., *Trade-off Optimization Method for Infrared Imaging System Based on Modification of λF/d.* IEEE Access, 2021. **9**: p. 16947-16956.

2. DiPirro, M., et al., *Cryocooling technologies for the Origins Space Telescope.* Journal of Astronomical Telescopes, Instruments, and Systems, 2021. **7**(1): p. 011008.

3. Wang, Q., et al., *Low-temperature grown vertically aligned carbon nanotube array for an optimal infrared bolometer.* Nanotechnology, 2021. **32**(50): p. 505719.

4. Zhu, H., et al., *Multispectral camouflage for infrared, visible, lasers and microwave with radiative cooling.* Nature Communications, 2021. **12**(1): p. 1805.

5. Wu, Y., et al., *Nanometallic antenna-assisted amorphous silicon waveguide integrated bolometer for mid-infrared.* Optics Letters, 2021. **46**(3): p. 677-680.

6. Wei, J., et al. *Uncooled Zero-Bias Graphene Mid-Infrared Detectors*. in *2021 IEEE 34th International Conference on Micro Electro Mechanical Systems (MEMS)*. 2021.

7. Roellig, T., et al., *Mid-infrared detector development for the Origins Space Telescope.* Journal of Astronomical Telescopes, Instruments, and Systems, 2020. **6**(4): p. 041503.

8. Mohammadi, E., M. Ghaffari, and N. Behdad, *Wide Dynamic Range, Angle-Sensing, Long-Wave Infrared Detector Using Nano-Antenna Arrays.* Scientific Reports (Nature Publisher Group), 2020. **10**(1).

9. Aburas, M., et al., *Smart windows – Transmittance tuned thermochromic coatings for dynamic control of building performance.* Energy and Buildings, 2021. **235**: p. 110717.

10. Garlisi, C., et al., *Multilayer thin film structures for multifunctional glass: Self-cleaning, antireflective and energy-saving properties.* Applied Energy, 2020. **264**: p. 114697.

11. Liu, C., et al., *Index-tunable anti-reflection coatings: Maximizing solar modulation ability for vanadium dioxide-based smart thermochromic glazing.* Journal of Alloys and Compounds, 2018. **731**: p. 1197-1207.

12. Gauthier, J.F. *Monitoring methane emissions at individual oil and gas sites with satellites: a new tool at the dawn of global transparency*. in *IGARSS 2020 - 2020 IEEE International Geoscience and Remote Sensing Symposium*. 2020.

13. Wang, A. and Y. Dan, *Mid-infrared plasmonic multispectral filters.* Scientific Reports, 2018. **8**(1): p. 11257.

14. Dandumont, C., et al., *Exoplanet detection yield of a space-based Bracewell interferometer from small to medium satellites.* Journal of Astronomical Telescopes, Instruments, and Systems, 2020. **6**(3): p. 035004.

15. Quanz, S., et al., *Exoplanet science with a space-based mid-infrared nulling interferometer*. SPIE Astronomical Telescopes + Instrumentation. Vol. 10701. 2018: SPIE.

16. Melkonian, J.-M., et al., *Long-wave infrared multi-wavelength optical source for standoff detection of chemical warfare agents.* Applied Optics, 2020. **59**(35): p. 11156-11166.

17. Zhao, Y., et al., *A Surface Geometry Model for LiDAR Depth Completion.* IEEE Robotics and Automation Letters, 2021. **6**(3): p. 4457-4464.

18. Zhang, J., et al., *Review of the overall parameter analysis of detection system of STSS*. Seventh Symposium on Novel Photoelectronic Detection Technology and Application 2020. Vol. 11763. 2021: SPIE.

19. Dong, L., et al., *Fabrication of hierarchical moth-eye structures with durable superhydrophobic property for ultra-broadband visual and mid-infrared applications.* Applied Optics, 2019. **58**(24): p. 6706-6712.

20. Lotz, M.R., et al., *Direct nanoimprinting of moth-eye structures in chalcogenide glass for broadband antireflection in the mid-infrared.* Optica, 2018. **5**(5): p. 557-563.

21. Pethuraja, G., et al., *Development of nanostructured antireflection coatings for infrared technologies and applications*. SPIE Optical Engineering + Applications. Vol. 10404. 2017: SPIE.

22. Schnee, V.P., N. Henry, and Q. Huynh, *Anti-reflective coating by 3D PDMS stamping using two-photon lithography master.* Optical Materials, 2021. **111**: p. 110715.

23. Stevens, L., et al., *Broadband antireflection Mie scatterers revisited—a solar cell and module analysis.* Optics Express, 2019. **27**(8): p. A524-A535.

24. Xu, Z., et al., *The Simons Observatory: metamaterial microwave absorber and its cryogenic applications.* Applied Optics, 2021. **60**(4): p. 864-874.

25. Yin, C., et al., *Al2O3 anti-reflection coatings with graded-refractive index profile for laser applications.* Optical Materials Express, 2021. **11**(3): p. 875-883.

26. Kraus, M., et al., *Combined ‘moth-eye’ structured and graded index-layer anti-reflecting coating for high index glasses.* Optics Express, 2019. **27**(24): p. 34655-34664.

27. Pickering, T., K. Shanks, and S. Sundaram, *Modelling technique and analysis of porous anti-reflective coatings for reducing wide angle reflectance of thin-film solar cells.* Journal of Optics, 2021. **23**(2): p. 025901.

28. Wang, X., et al., *Polarization-stabilized tunable VCSEL with internal-cavity sub-wavelength grating.* Optics Express, 2019. **27**(24): p. 35499-35511.

29. Zhang, Z.M., *Nano/microscale heat transfer*. 2007: Springer.

30. Chen, N.-K., S. Chi, and S.-M. Tseng, *Wideband tunable fiber short-pass filter based on side-polished fiber with dispersive polymer overlay.* Optics Letters, 2004. **29**(19): p. 2219-2221.

31. Chen, Y., et al., *Compact optical short-pass filters based on microfibers.* Optics Letters, 2008. **33**(21): p. 2565-2567.

32. Heenkenda, R., K. Hirakawa, and A. Sarangan, *Tunable optical filter using phase change materials for smart IR night vision applications.* Optics Express, 2021. **29**(21): p. 33795-33803.

33. Habib, M. and A. Ullah. *Simulation of near Infrared interference bandpass filters for spectroscopic applications*. in *2016 International Conference on Computing, Electronic and Electrical Engineering (ICE Cube)*. 2016.

34. Jen, Y.-J. and M.-J. Lin, *Design and Fabrication of a Narrow Bandpass Filter with Low Dependence on Angle of Incidence.* Coatings, 2018. **8**(7): p. 231.

35. Kumar, S., et al., *Near-infrared bandpass filters from Si/SiO2 multilayer coatings.* Optical Engineering, 1999. **38**(2).

36. Shahrokhabadi, H., et al., *A compact sharp-edge wide bandpass near-infrared filter based on graded-index sinusoidally corrugated photonic crystal.* Physics Letters A, 2020. **384**(11): p. 126235.

37. Tavousi, A., M.A. Mansouri-Birjandi, and M. Janfaza, *Optoelectronic application of graphene nanoribbon for mid-infrared bandpass filtering.* Applied Optics, 2018. **57**(20): p. 5800-5805.

38. El-Bashir, S.M., et al., *Designing of PVA/Rose Bengal long-pass optical window applications.* Results in Physics, 2017. **7**: p. 1238-1244.

39. Baetens, R., B.P. Jelle, and A. Gustavsen, *Properties, requirements and possibilities of smart windows for dynamic daylight and solar energy control in buildings: A state-of-the-art review.* Solar Energy Materials and Solar Cells, 2010. **94**(2): p. 87-105.

40. Magden, E.S., et al., *Transmissive silicon photonic dichroic filters with spectrally selective waveguides.* Nature Communications, 2018. **9**(1): p. 3009.

41. Jakobs, S. and U. Schallenberg, *High-precision longpass filter arrays for miniature spectrometers*. Optical Systems Design. Vol. 5250. 2004: SPIE.

42. Yan, W. and M. Qiu, *Two-dimensional optical edge detection.* Nature Photonics, 2020. **14**(5): p. 268-269.

43. Zhou, J., et al., *Optical edge detection based on high-efficiency dielectric metasurface.* Proceedings of the National Academy of Sciences, 2019. **116**(23): p. 11137.

44. Moharam, M.G., et al., *Formulation for stable and efficient implementation of the rigorous coupled-wave analysis of binary gratings.* Journal of the Optical Society of America A, 1995. **12**(5): p. 1068-1076.

45. Qiao, P., et al., *Theory and design of two-dimensional high-contrast-grating phased arrays.* Optics Express, 2015. **23**(19): p. 24508-24524.

46. Rumpf, R.C. and E.G. Johnson, *Modeling fabrication to accurately place GMR resonances.* Optics Express, 2007. **15**(6): p. 3452-3464.

47. Zhao, B., et al., *Thermophotovoltaic emitters based on a two-dimensional grating/thin-film nanostructure.* International Journal of Heat and Mass Transfer, 2013. **67**: p. 637-645.

48. Chen, G., *Nanoscale Energy Transport and Conversion: A Parallel Treatment of Electrons, Molecules, Phonons, and Photons*. 2005: Oxford University Press.

49. Li, H.H., *Refractive index of alkali halides and its wavelength and temperature derivatives.* Journal of Physical and Chemical Reference Data, 1976. **5**(2): p. 329-528.

50. Zhang, X., et al., *Complex refractive indices measurements of polymers in visible and near-infrared bands.* Applied Optics, 2020. **59**(8): p. 2337-2344.

51. Blankenship, M., K. Adams, and R. Zhang, *Gradient-index metasurface multilayer for quasioptical coupling of infrared detectors.* Optical Engineering, 2021. **60**(10): p. 107102.

52. Gottlieb, D. and C.-W. Shu, *On the Gibbs phenomenon and its resolution.* SIAM review, 1997. **39**(4): p. 644-668.

53. Maystre, D., *Theory of Wood's anomalies*, in *Plasmonics*. 2012, Springer. p. 39-83.

54. Zhang, R.Z. and Z.M. Zhang, *Validity of effective medium theory in multilayered hyperbolic materials.* Journal of Quantitative Spectroscopy and Radiative Transfer, 2017. **197**: p. 132-140.

55. Hughes, T.W., et al., *A perspective on the pathway toward full wave simulation of large area metalenses.* Applied Physics Letters, 2021. **119**(15): p. 150502.

56. Sullivan, D., *Electromagnetic Simulation Using the FDTD Method, Second Edition.* IEEE Microwave Theory Tech Soc, 2013.

57. Hecht, E., *Optics*. 2017: Pearson Education, Incorporated.

58. Lumerical, A. *Understanding Mesh Refinement and Conformal Mesh in FDTD*. 2021 [cited 2022 March 30,2022]; Available from: https://support.lumerical.com/hc/en-us/articles/360034382594-Understanding-Mesh-Refinement-and-Conformal-Mesh-in-FDTD.

59. Gibson, N.L., *Numerical Methods for Maxwell's Equations*. 2015: Oregon State University.